processes

MDPI

Article

Electrochemical Performance of Aluminum Doped $Ni_{1-x}Al_xCo_2O_4$ Hierarchical Nanostructure: Experimental and Theoretical Study

Deepa Guragain [1], Romakanta Bhattarai [1], Jonghyun Choi [2], Wang Lin [2], Ram Krishna Gupta [2], Xiao Shen [1], Felio A. Perez [1] and Sanjay R. Mishra [1,*]

[1] Department of Physics and Materials Science, The University of Memphis, Memphis, TN 38152, USA; ddeepag13@gmail.com (D.G.); rbhttri1@memphis.edu (R.B.); xshen1@memphis.edu (X.S.); fperez@memphis.edu (F.A.P.)

[2] Department of Chemistry, Pittsburg State University, Pittsburg, KS 66762, USA; jonghyunchoi09@gmail.com (J.C.); wang.lin@gus.pittstate.edu (W.L.); rgupta@pittstate.edu (R.K.G.)

* Correspondence: srmishra@memphis.edu

Abstract: For electrochemical supercapacitors, nickel cobaltite ($NiCo_2O_4$) has emerged as a new energy storage material. The electrocapacitive performance of metal oxides is significantly influenced by their morphology and electrical characteristics. The synthesis route can modulate the morphological structure, while their energy band gaps and defects can vary the electrical properties. In addition to modifying the energy band gap, doping can improve crystal stability and refine grain size, providing much-needed surface area for high specific capacitance. This study evaluates the electrochemical performance of aluminum-doped $Ni_{1-x}Al_xCo_2O_4$ ($0 \leq x \leq 0.8$) compounds. The $Ni_{1-x}Al_xCo_2O_4$ samples were synthesized through a hydrothermal method by varying the Al to Ni molar ratio. The physical, morphological, and electrochemical properties of $Ni_{1-x}Al_xCo_2O_4$ are observed to vary with Al^{3+} content. A morphological change from urchin-like spheres to nanoplate-like structures with a concomitant increase in the surface area, reaching up to 189 m^2/g for x = 0.8, was observed with increasing Al^{3+} content in $Ni_{1-x}Al_xCo_2O_4$. The electrochemical performance of $Ni_{1-x}Al_xCo_2O_4$ as an electrode was assessed in a 3M KOH solution. The high specific capacitance of 512 F/g at a 2 mV/s scan rate, 268 F/g at a current density of 0.5 A/g, and energy density of 12.4 Wh/kg was observed for the x = 0.0 sample, which was reduced upon further Al^{3+} substitution. The as-synthesized $Ni_{1-x}Al_xCo_2O_4$ electrode exhibited a maximum energy density of 12.4 W h kg^{-1} with an outstanding high-power density of approximately 6316.6 W h kg^{-1} for x = 0.0 and an energy density of 8.7 W h kg^{-1} with an outstanding high-power density of approximately 6670.9 W h kg^{-1} for x = 0.6. The capacitance retention of 97% and 108.52% and the Coulombic efficiency of 100% and 99.24% were observed for x = 0.0 and x = 0.8, respectively. First-principles density functional theory (DFT) calculations show that the band-gap energy of $Ni_{1-x}Al_xCo_2O_4$ remained largely invariant with the Al^{3+} substitution for low Al^{3+} content. Although the capacitance performance is reduced upon Al^{3+} doping, overall, the Al^{3+} doped $Ni_{1-x}Al_xCo_2O_4$ displayed good energy, powder density, and retention performance. Thus, Al^{3+} could be a cost-effective alternative in replacing Ni with the performance trade off.

Keywords: hydrothermal; $Ni_{1-x}Al_xCo_2O_4$; electrochemical; cyclic voltammetry; the specific capacitance

check for updates

Citation: Guragain, D.; Bhattarai, R.; Choi, J.; Lin, W.; Gupta, R.K.; Shen, X.; Perez, F.A.; Mishra, S.R. Electrochemical Performance of Aluminum Doped $Ni_{1-x}Al_xCo_2O_4$ Hierarchical Nanostructure: Experimental and Theoretical Study. *Processes* **2021**, *9*, 1750. https://doi.org/10.3390/pr9101750

Academic Editor: Domenico Frattini

Received: 3 August 2021
Accepted: 22 September 2021
Published: 30 September 2021

1. Introduction

Researchers are actively engineering an efficient, clean, and cost-effective electrode for better electrochemical performance [1]. Conventional capacitors and batteries are broadly exploited by energy storage devices [2]. Previously, secondary batteries were suitable electrical energy storage devices, but they were not very satisfactory because of their smaller power density, presence of toxic waste substances, and shorter lifetime [3]. On the other hand, conventional capacitors display high power density compared to a battery, but because of their lower energy density, researchers are interested in advanced energy storing devices that mitigate the demerits of both battery and capacitor. The energy gap between batteries and capacitors can be bridged by a supercapacitor (SC) [4]. SC electrode materials must have a large specific surface area, controlled porosity, high electronic conductivity, suitable electroactive sites, high thermal stability, low raw material costs, and ease of manufacture [5]. Supercapacitors have recently attracted attention due to their quick charging/discharging, high power density, wide range of working temperatures, high efficiency, and extended lifespans [6]. SCs are of three types: (i) electrical double layer capacitance (EDLCs) examples are highly porous carbon materials, (ii) pseudocapacitor (PCs) examples are transition metal oxides and conducting polymers, and (iii) hybrid capacitor examples are battery type hybrid devices such as the lithium-ion capacitor [7]. EDLCs store electrical energy in the electric double layer, which occurs at the interface between the electrode's active material and the electrolyte by an electrostatic accumulation process. In EDLCs, energy density becomes lower (between 3 and 6 Wh/Kg), and specific capacitance is restricted because of the specific surface area of the active electrode material [8]. The ionic double layer's fast diffusion provides a very rapid discharge profile and hence high-power densities. PCs, on the other hand, are caused by reversible Faradaic processes at the electrode surface, which cause charge storage [9]. Moreover, in PCs, the electrochemical process occurs near the surface of the active electrode material. Thus, it can give specific capacitance 10–100 times greater than that provided by EDLCs [10]. Moreover, hybrid capacitors are a combination of both EDLCs and PCs. Usually, hybrid capacitor electrodes are made from (1) both EDLCs materials and PCs materials; symmetric geometry (2) with one EDLCs electrode and other PCs or battery type electrode; and asymmetric geometry (3) with an asymmetric structure with one PC electrode and another rechargeable battery type electrode [7].

In a pseudocapacitor, a redox reaction takes place between the active electrode material and the electrolyte. Various kinds of transition metal oxides having higher theoretical specific capacitance, such as RuO_2 [11], MnO_2 [12], NiO [13], $Ni(OH)_2$ [14], CuO [15], Co_3O_4 [16], and $Co(OH)_2$ [17], have been investigated as an active electrode material. However, their poor electronic conductivity [18,19], lower cyclic performance [20,21], and substantial volume change during the charge/discharge process [22] demand the development of nanostructured materials to meet the increasing and urgent demands for energy storing devices. Recently, mixed-transition-metal-oxides (MTMOs), $A_xB_{3-x}O_4$ materials have emerged with promising applications for electrodes. The MTMOs with A and B metal ions can provide many oxidation states for efficient redox charge reactions [23]. Nickel cobaltite ($NiCo_2O_4$) is one of the most valuable electrode materials studied because of its high theoretical specific capacitance, lower cost, low toxic nature, good redox activity, higher electrical conductivity, and environmentally benign nature [24]. $NiCo_2O_4$ offers high specific capacitance due to the presence of Ni and Co ions together, which are responsible for producing higher electrochemical activity and electrical conductivity [25]. $NiCo_2O_4$ is a spinel-type, AB_2O_4, binary metal oxide where nickel cations occupy octahedral sites and cobalt cations are randomly distributed on both tetrahedral and octahedral sites [26].

Doped $NiCo_2O_4$ with various transition metals, e.g., $Ni_{1-x}Ru_xCo_2O_4$ [27], $Ni_{1-x}Mn_xCo_2O_4$ [28], $Ni_{1-x}Cr_xCo_2O_4$ [29], $Ni_{1-x}Zn_xCo_2O_4$ [30], $Ni_{1-x}Fe_xCo_2O_4$ [31], and $Ni_{1-x}Ca_xCo_2O_4$ [32], have been studied to understand the effect on morphology and their electrochemical performance. This paper describes a simple hydrothermal method for making Al^{3+} doped $NiCo_2O_4$, i.e., $Ni_{1-x}Al_xCo_2O_4$. The study systematically assesses the effect of Al^{3+} doping on the crystal structure, morphology, chemical composition, and electrochemical performance of $Ni_{1-x}Al_xCo_2O_4$. Aluminum ion substitution is favored because of its inexpensive cost, large abundance, non-toxic nature, and superior corrosion resistance. First-principles density functional theory (DFT) calculations were employed to assess the energy band-gap of the doped $Ni_{1-x}Al_xCo_2O_4$.

2. Experimental

2.1. Synthesis

The required high purity nitrate salts, viz. $Al(NO_3)_2.6H_2O$, $Co(NO_3)_2.6H_2O$, and $Ni(NO_3)_2.6H_2O$, were purchased from Sigma Aldrich (St. Louis, MO, USA). Table 1 lists the required amount of precursor salts needed to prepare $Ni_{1-x}Al_xCo_2O_4$. The nitrate salts were dissolved in 35 mL of water with a fixed amount of Urea ($CO(NH_2)_2$) and stirred for 30 min. The solution was then transferred to a 45 mL Teflon-lined autoclave and maintained at 190 °C for 12 h, followed by a natural cooling to room temperature. The precipitates were washed with distilled water and acetone several times by centrifugation and then dried for 12 h at 80 °C. After this, the as derived metal hydroxide composite particles were calcined at 350 °C in the air for 3.5 h.

Table 1. Stoichiometry of chemicals used in the synthesis of $Ni_{1-x}Al_xCo_2O_4$.

$Ni_{1-x}Al_xCo_2O_4$, x	$Co(NO_3)_2{\cdot}6H_2O$ (gm)	$Ni(NO_3)_2{\cdot}6H_2O$ (gm)	$Al(NO_3)_2{\cdot}6H_2O$ (gm)	Urea (gm)
0.0	2.420	1.209	0.000	1.497
0.2	2.485	0.993	0.320	1.497
0.4	2.550	0.765	0.658	1.497
0.6	2.620	0.525	1.016	1.497
0.8	3.850	0.384	1.985	1.497

2.2. Characterization

X-ray diffraction (XRD) was used to examine the crystalline structure of calcined powder using a Bruker D8 Advance X-ray diffractometer (Bruker, Billerica, MA, USA). The surface morphology of prepared samples was studied by a scanning electron microscope (SEM) (at 10 keV using Phenom, Oak Park, CA, USA). Autosorb (Quantachrome, Boynton Beach, FL 33426, USA, model No. AS1MP) was used to quantify specific surface area and pore volume at 77K using nitrogen as the adsorbing gas. The Brunauer–Emmett–Teller (BET) method was used to measure the specific surface area of as-prepared samples. Also, surface area, average pore volume, and pore radius were obtained from the Barret–Joyner–Halenda (BJH) model. Between 400 and 1000 cm^{-1}, FTIR spectra were acquired using an FTIR spectrometer (Nicolet iS10, Thermo Fisher Scientific, Waltham, MA, USA). The x-ray photoelectron spectrometer (Thermo Scientific K-alpha, XPS) equipped with a monochromatic X-ray source at 1486.6 eV, corresponding to the Al K_α line, was employed to collect XPS data (for the brevity XPS spectra not shown). The atomic weight percent of elements was determined using XPS.

The working electrode was prepared using nickel foam. Nickel foam was first cleaned with acetone and 3 M HCl solution for 10 min, which helped remove the oxide layer from the nickel foam's surface. After washing and drying the nickel foam, the working electrode was made by combining 80 wt.% of the synthesized powder, 10 wt. % of acetylene black, and 10 wt. % of polyvinylidene difluoride (PVDF) with N-methyl pyrrolidinone (NMP). The slurry paste was obtained after thoroughly mixing the components and pasted onto the nickel foam. The prepared electrode on nickel foam was placed in a vacuum oven at a temperature of 60 °C for 10 h. The actual sample loading on nickel foam was determined by weighing the nickel foam before and after loading the nickel foam sample using an analytical balance (MS105DU, Mettler Toledo, max. 120 g, 0.01 mg of resolution). A platinum wire counter electrode, a saturated calomel electrode (SCE) as a reference electrode, and pasted samples on nickel foam as a working electrode were utilized in the electrochemical cell. The electrochemical performance of the electrode was assessed in 3 M KOH as an electrolyte. The electrochemical performance of the as-prepared electrode was evaluated using cyclic voltammetry (CV), galvanostatic charge-discharge techniques, and electrochemical impedance spectroscopy (EIS) by using a Versastat4-500 electrochemical workstation (Princeton Applied Research, Oak Ridge, TN, USA).

2.3. DFT Study

First-principles density functional theory (DFT) calculations were performed using the Perdew–Burke–Ernzerhof (PBE) [33] exchange-correlation functional for self-consistent calculations and geometry optimization along with the advanced hybrid functional HSE06 method to find the electronic density of states of the $Al_xNi_{1-x}Co_2O_4$ structure. The variable x ranges from 0 to 1 with a step of 0.25. Calculations were performed using VASP [34] (Vienna ab initio simulation package) with the projected augmented wave (PAW) [35] type pseudo-potential and the plane-wave basis set. The exchange and correlation part for the HSE calculations was described by hybrid functional [36] containing 40% Hartree–Fock exchange. We used a 4 × 4 × 2 k-points mesh centered at the Gamma point with a plane wave cutoff of 400 eV, which is enough for the self-consistent calculation. The global break condition for the electronic and ionic self-consistent (SC) loop was set to be 10^{-4} eV and 10^{-3} eV, respectively.

3. Results and Discussion

The room temperature powder XRD patterns of $Ni_{1-x}Al_xCo_2O_4$ samples are shown in Figure 1. The XRD patterns of the as-synthesized doped $Ni_{1-x}Al_xCo_2O_4$ are almost identical and can be assigned to $NiCo_2O_4$ (ICDD card no.02-0770). The diffraction peaks are located at 18.9°, 31.3°, 36.8°, 38.4°, 44.5°, 55.4°, 59.4°, and 65.2° can be assigned to the (111), (220), (311), (222), (400), (422), (511), and (440) agreeing with the standard crystallographic pattern of spinel $NiCo_2O_4$ phase respectively [37]. The absence of impurities in the XRD patterns confirms the complete dissolution of Al^{3+} into the $Ni_{1-x}Al_xCo_2O_4$ compound. The lattice parameter of $Ni_{1-x}Al_xCo_2O_4$ is listed in Table 2. As expected, the lattice parameter of $Ni_{1-x}Al_xCo_2O_4$ decreases with the content x due to Al^{3+} (r_{ion} ~0. 535 nm) replacing a bigger Ni ion (r_{ionic} ~0.6 nm). The average crystallite size of the $NiCo_2O_4$ calculated using Scherrer's formula [38] is listed in Table 2. The average crystallite size of $Ni_{1-x}Al_xCo_2O_4$ falls within the range of 12.28 nm for x = 0.8 to 16.52 nm for x = 0.2. Moreover, sharp diffraction peaks indicated the crystalline nature of the calcined $Ni_{1-x}Al_xCo_2O_4$ nanostructures. The aluminum content in $Ni_{1-x}Al_xCo_2O_4$ as determined via XPS (XPS study is not reported here) is listed in Table 2 and is within the accepted range of stoichiometry of the compound.

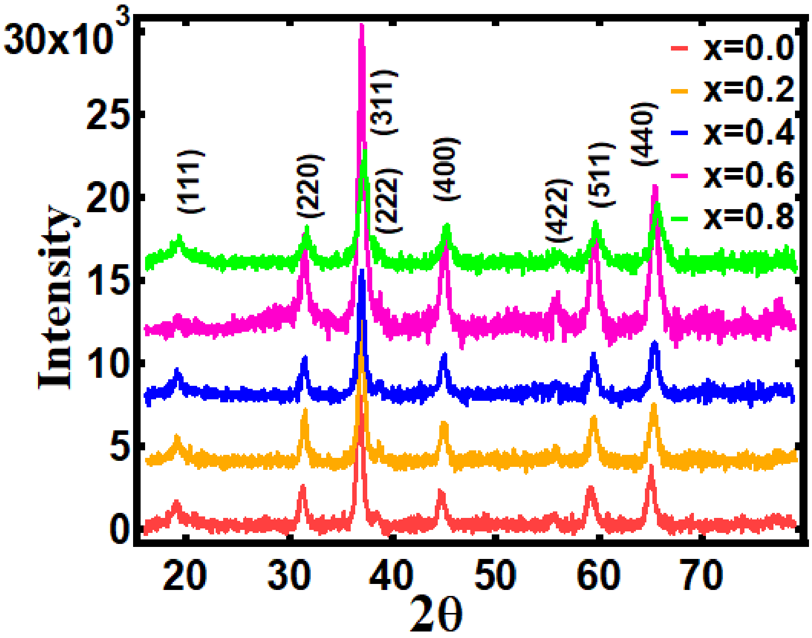

Figure 1. X-ray diffraction pattern for $Ni_{1-x}Al_xCo_2O_4$.

Table 2. Surface area parameters derived from the adsorption-desorption curve, crystallite size obtained using Scherrer's formula, lattice parameter obtained from XRD refinement, and Al^{3+} content was obtained from the XPS analysis of $Ni_{1-x}Al_xCo_2O_4$ compound.

$Ni_{1-x}Al_xCo_2O_4$, x	Al Content Determined via XPS	BET Surface Area (m^2/g)	BJH Surface Area (m^2/g)	BJH Avg. Pore Radius (nm)	BJH Avg. Pore Volume (cc/g)	Lattice Parameter, a (Å)	Crystallite Size (nm)
0.0	0.00	81.74	89.09	1.419	0.239	8.0983	13.212
0.2	0.37	83.16	126.13	1.423	0.183	8.0804	16.525
0.4	0.57	107.19	120.26	1.522	0.192	8.0666	13.804
0.6	0.79	106.29	128.81	2.144	0.194	8.0585	14.776
0.8	0.89	189.00	354.83	1.593	0.276	8.0449	12.286

Figure 2 shows the SEM images of $Ni_{1-x}Al_xCo_2O_4$ as a function of Al^{3+} content. Figure 2 shows the gradual evolution of $Ni_{1-x}Al_xCo_2O_4$ nanostructures from an urchin-like architecture for x = 0.0 to nanoplates for x = 0.8. It is evident that the initial urchin whiskers slowly merge and morph into a plate-like structure with increasing Al content. The morphology of $Ni_{1-x}Al_xCo_2O_4$ is dependent on the Al^{3+} content in the sample. Usually, the morphology of hierarchal nanostructures depends on the synthesis techniques and urea concentration [4]. As a dispersing agent, urea helps avoid agglomeration by finely separating nanoparticles and plays a vital role in controlling the particles' morphology [39–41].

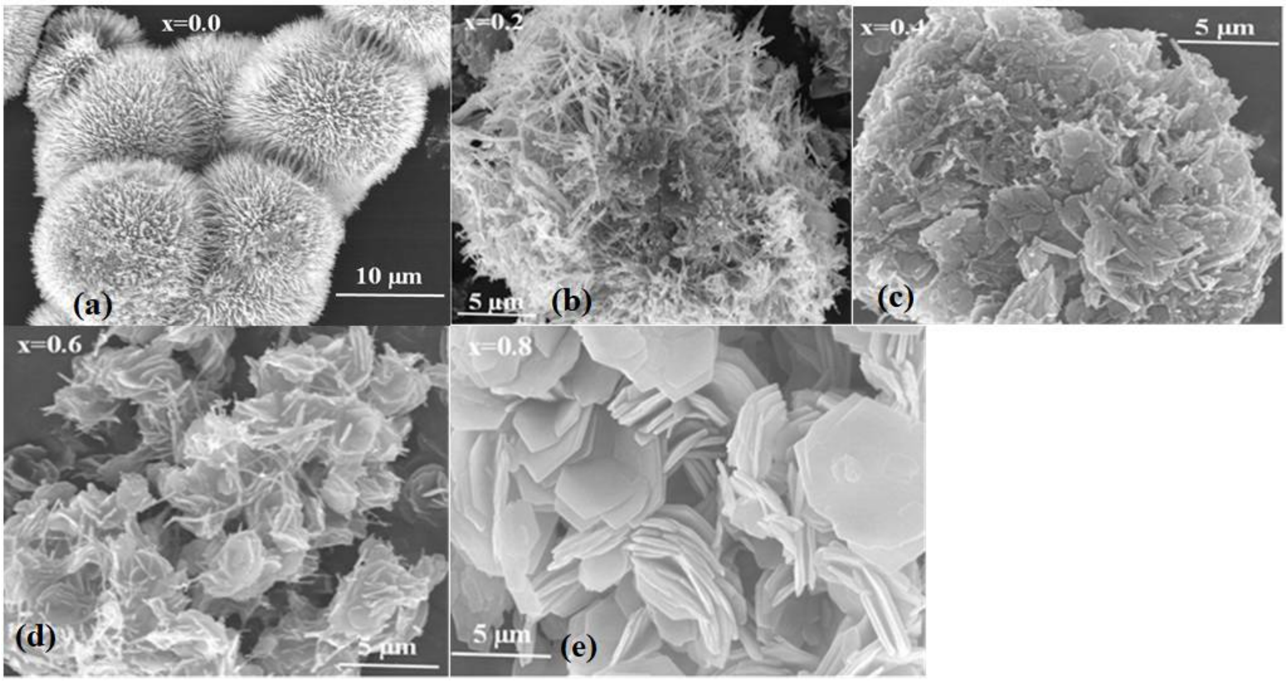

Figure 2. SEM images for $Ni_{1-x}Al_xCo_2O_4$ samples (**a**) x = 0, (**b**) x = 0.2, (**c**) x = 0.4, (**d**) x = 0.6, and (**e**) x = 0.8.

Furthermore, NH_3 reacts with water to form NH_4^+ and OH^-, and CO_2 hydrolyzes to form Co_3^{2-} ions [42]. Tiny crystalline nuclei are created during the oxide crystal development phase, and nanoparticles of this oxide are precipitated by a rise in pH caused by NH_4^+ ions generated from NH_3 owing to urea breakdown at higher temperatures [43,44]. Urea's hydrolysis leads to a rise in the pH due to the increased release of NH_4^+ in the solution [45]. The urea hydrolysis progresses slowly at milder circumstances and at a certain urea level, and the basic solution undergoes supersaturation of the metal-hydroxide species [46].

Figure 3a shows N_2 adsorption/desorption measurements were performed at 77 K between relative pressures of P/P_o ~ 0.029 to 0.99. From these curves, BET-specific surface areas and corresponding pore sizes were calculated by the BJH method for all $Ni_{1-x}Al_xCo_2O_4$

($0 \leq x \leq 0.8$). Figure 2c inset shows the pore distribution. These curves show the largest number of pores distribution at around 3 nm for all $Ni_{1-x}Al_xCo_2O_4$. This pore distribution lies between ~2.0 and 6.0 nm, a range best suited to electrode materials [46]. The larger pore volume helps boost the diffusion kinetics inside the electrode material [40,46,47]. Table 2 lists the measured BJH pore radius, volume, and BET surface area of $Ni_{1-x}Al_xCo_2O_4$ samples. The high surface area of samples, in the range of 81.74–189 m^2/g, indicates that the hydrated electrolyte ions could have an increased contact area at the electrolyte/electrode surface for the Faradaic redox reaction [48,49].

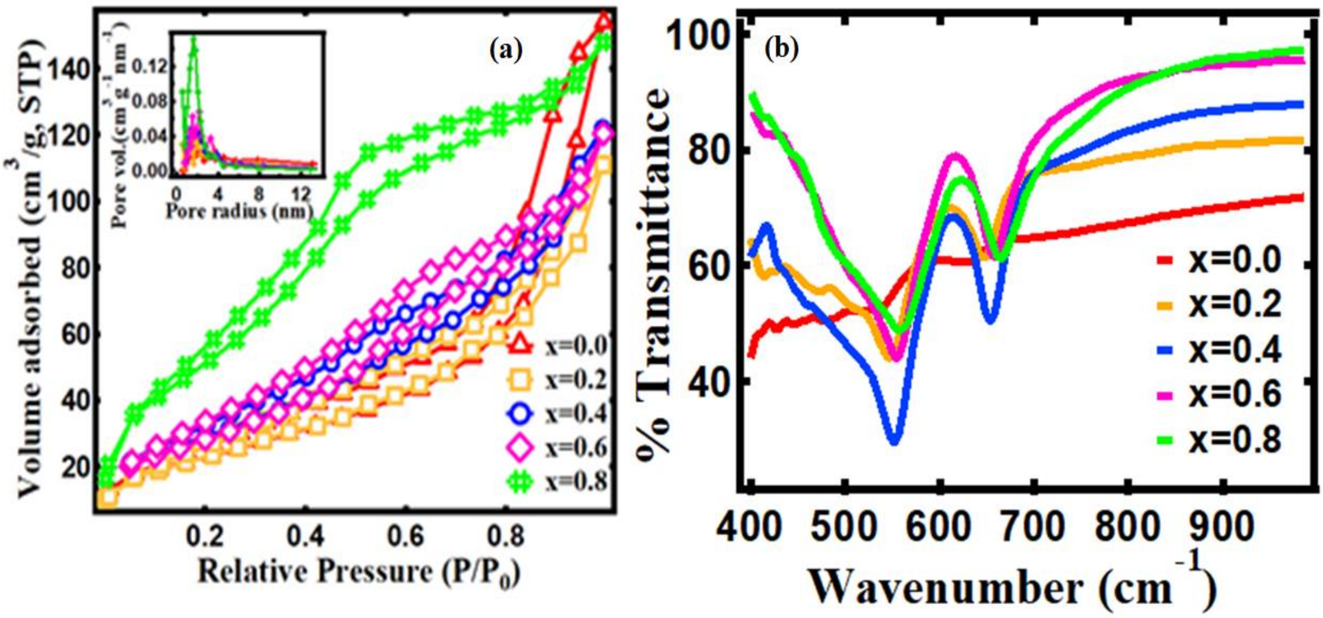

Figure 3. (**a**) Adsorption-desorption curves and inset pore volume distribution for $Ni_{1-x}Al_xCo_2O_4$, and (**b**) FTIR of $Ni_{1-x}Al_xCo_2O_4$.

The FTIR spectrum Figure 3b shows two different bands arising from the stretching vibrations of the metal-oxygen bonds at 534.2 (ν_1) and 628.7 (ν_2) cm^{-1} [1]. For the crystal structure of $NiCo_2O_4$, the ν_1 band is attributed to M-O (M = Ni) bond vibrations in octahedral coordination, whereas the ν_2 band is attributed to M-O (M-Co) bond vibrations in tetrahedral coordination. The stretching vibration of Co^{3+}-O^{2-} in the octahedral sites is shown by the FTIR spectrum at 534.2 cm^{-1}, and the vibration of Ni^{2+}-O^{-} at the tetrahedral sites is indicated by the FTIR spectrum at 628.7 cm^{-1} for $NiCo_2O_4$, respectively [50]. The presence of these vibration bands indicates that pure phase spinel $NiCo_2O_4$ nanostructures have formed. Table 3 lists the band positions for the tetrahedral and octahedral sites of the compound. Aluminum doping brings the shift of the stretching peak towards the right with an increase in Al^{3+} content. As the vibrational frequency is inversely proportional to the mass, the increase in vibrational frequency with Al^{3+} is expected due to the lower atomic weight of Al^{3+} replacing the Ni ion.

Table 3. Two distinct band positions from FTIR spectrum for $Ni_{1-x}Al_xCo_2O_4$ samples.

$Ni_{1-x}Al_xCo_2O_4$, x	ν_1 (cm^{-1})	ν2 (cm^{-1})
0.0	534.2	628.7
0.2	544.0	645.2
0.4	551.0	652.7
0.6	553.6	653.9
0.8	556.1	665.1

Cyclic voltammetry (CV) and galvanostatic charge-discharge (GCD) measurements give the electrochemical performance of $Ni_{1-x}Al_xCo_2O_4$ nanostructures. Figure 4a–e shows the cyclic voltammograms obtained at different scan rates (2–300 mV/s) in a voltage window of 0–0.6 V (vs. SCE). The Faradaic reaction for $NiCo_2O_4$, x = 0 is given by the equation below [51,52].

$$MO + OH^- \leftrightarrow MOOH + e^-$$

$$NiCo_2O_4 + OH^- + H_2O \leftrightarrow NiOOH + 2CoOOH + e^-$$

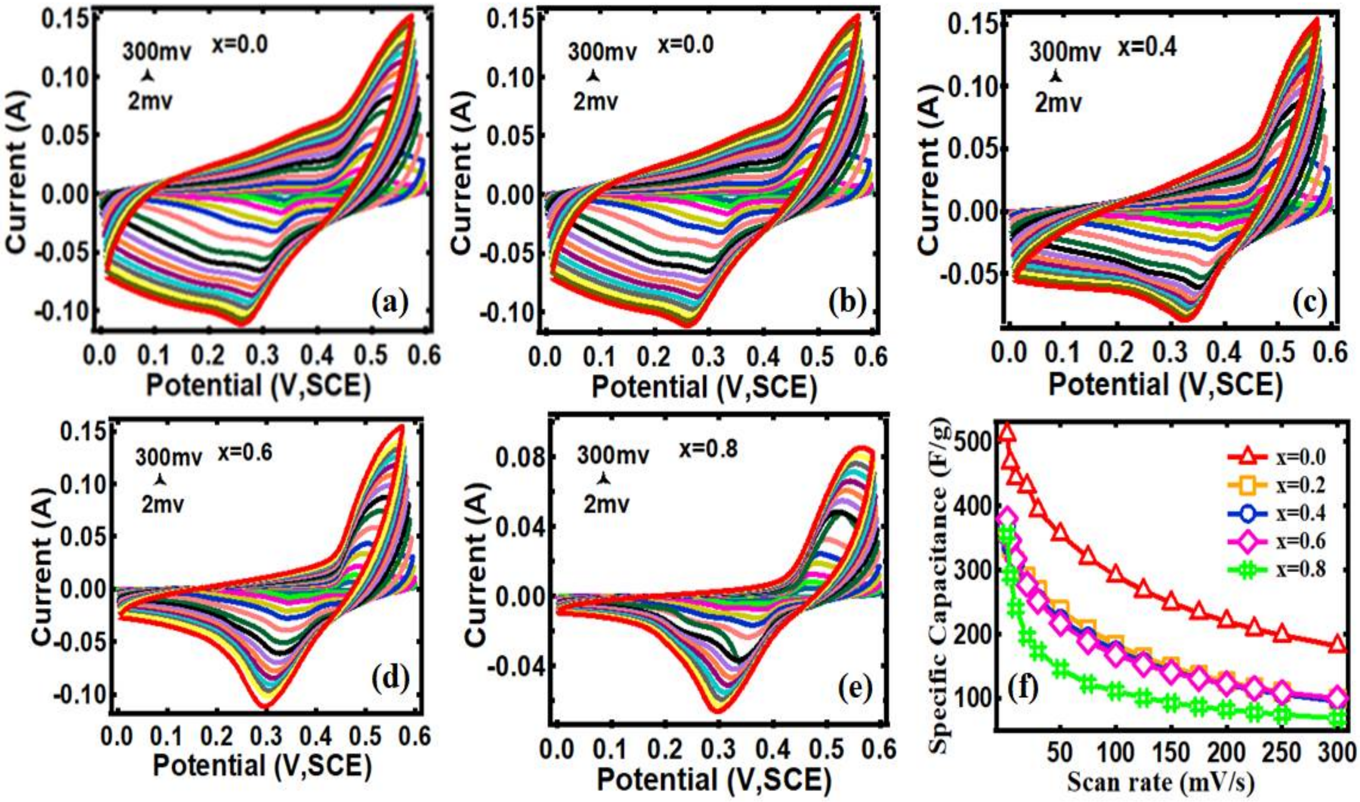

Figure 4. (**a**–**e**) are cyclic voltammetry curves of $Ni_{1-x}Al_xCo_2O_4$, electrode obtained in the scan range of 5 mV/s to 300 mV/s measured in 3M KOH electrolytes. Figure (**f**) specific capacitance vs. scan rate.

In both the cathodic and anodic scans, there are noticeable oxidation and reduction peaks [53]. Obtained non-rectangular and unsymmetric CV curves indicate the pseudocapacitive nature of electrodes [54]. The CV curves of $Ni_{1-x}Al_xCo_2O_4$ show no extra redox peaks, implying that $Ni_{1-x}Al_xCo_2O_4$ redox processes are very similar to $NiCo_2O_4$ redox processes. The peaks are due to the redox reaction related to M-O/M-O-OH, where M stands for Ni or Co ions [55]. A positive shift in oxidation peak potential and a negative shift in reduction peak potential are found as scan rate increases [56]. This PC characteristic is derived from the Faradaic redox reaction related to the reversible reaction of Ni^{2+}/Ni^{3+} and Co^{3+}/Co^{4+} transitions. Figure 5a–e shows the cyclic stability curves of $Ni_{1-x}Al_xCo_2O_4$ measured up to 2000 cycles without any change in the position of redox peaks.

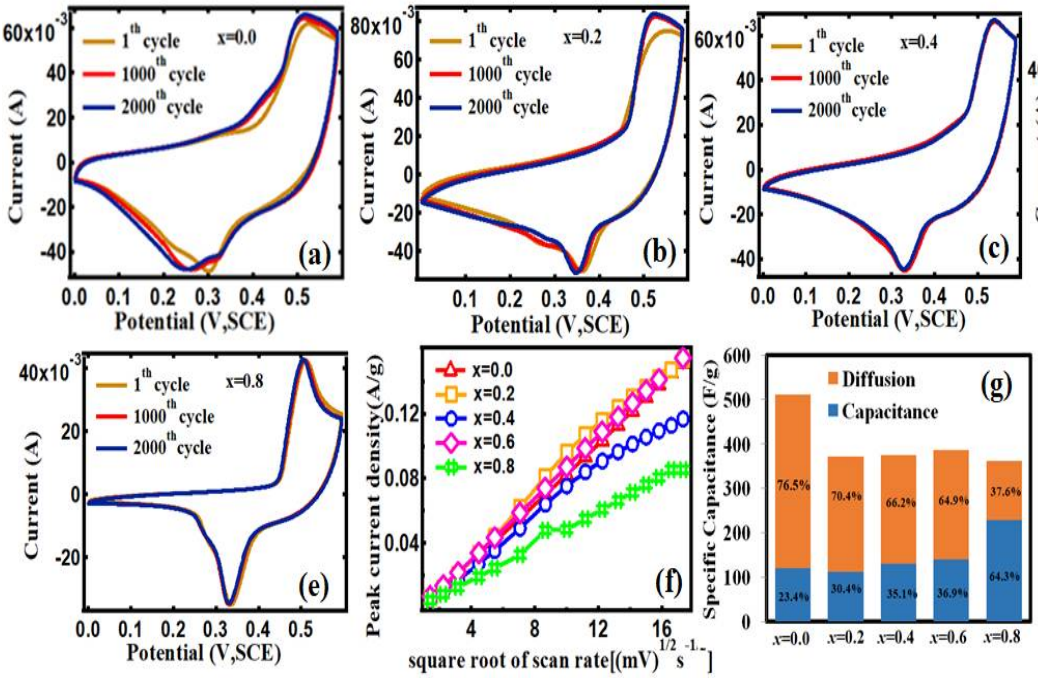

Figure 5. (**a**–**e**) are cyclic stability curves of $Ni_{1-x}Al_xCo_2O_4$ measured up to 2000 cycles in 3M KOH electrolyte, (**f**) peak current vs. (scan rate)$^{1/2}$, and (**g**) diffusion and capacitive contribution to the specific capacitance.

The Randles–Sevcik plots of the $Ni_{1-x}Al_xCo_2O_4$ samples are shown in Figure 5f. When the scan rate is increased from 2 to 300 mV s^{-1}, the anodic peak current (I_{pa}) and the cathodic peak current (I_{pc}) both increase. More precisely, the Randles–Sevcik equation shows that both I_{pa} and I_{pc} change linearly with the square root of the scan rate ($\nu^{1/2}$) [57,58]. These results suggest that the electrode–electrolyte interface's redox events are rapid, quasi-reversible, and only limited by electrolyte diffusion [59]. The positive shift of oxidation peak and negative shift of reduction peak potential indicate relatively low electrode materials resistance and good electrochemical reversibility [1].

The calculation of specific capacitance was done from CV curves using the equation below [60]:

$$C_{sp} = \frac{\int_{V_1}^{V_2} I * V * dV}{m * v * (V_2 - V_1)} \tag{1}$$

where I (A) is current, m (g) is the mass of the active material, v (mV/s) is the scan rate, V_1 and V_2 (V) are the start and end voltage of the CV scan.

Figure 4f shows the C_{sp} of $Ni_{1-x}Al_xCo_2O_4$ samples as a function of scan rates. The obtained values of C_{sp} for $Ni_{1-x}Al_xCo_2O_4$ nanostructures are 512, 368, 371, 380, and 356 F/g at a scan rate of 2 mV/s for $Ni_{1-x}Al_xCo_2O_4$ x = 0.0, 0.2, 0.4, 0.6, and 0.8, respectively. Compared to all $Ni_{1-x}Al_xCo_2O_4$ nanostructures, $NiCo_2O_4$ x = 0.0 exhibited the highest specific capacitance at all scan rates with a maximum value of 512 F/g at 2 mV/s. The higher electrochemical utilization and high electroactive surface area of the synthesized nanostructure occur for $Ni_{1-x}Al_xCo_2O_4$, $x = 0$. The observed decrease in C_{sp} with Al^{3+} substitution suggests that in the presence of Al^{3+}, the Ni and Co in $Ni_{1-x}Al_xCo_2O_4$ may not behave synergistically as an effective Faradaic charging site as compared with the Ni and Co sites in $NiCo_2O_4$. Moreover, it can be deduced that, with the increase in Al^{3+} content, overall effective redox sites have decreased, which leads to a decrease in the specific capacitance.

The total charge storage process is affected by factors such as the Faradaic contribution from the insertion process of electrolyte ions, the Faradaic contribution from the charge-transfer process, and due to the high surface area, the contribution from both pseudocapacitance and the non-Faradaic contribution from the double layer effects [61].

CV data are analyzed at different scan rates and can characterize capacitive effects by equation [62,63].

$$I = av^b \tag{2}$$

where the peak current is I (A), the scan rate is v (mV/s), and a and b are adjustable parameters. The value of b specifies the charge storage mechanism. If b = 1, it indicates a surface-controlled reaction that the capacitive surface mechanism is dominant, and if b = 0.5, it indicates a diffusion-controlled Faradaic reaction during the charge storage mechanism [64]. Figure 5f shows the peak current vs. square root of the scan rate curve. These curves are fitted with the Equation (2) which gives values of $b \sim 0.6239$, 0.6398, 0.6218, 0.6134, and 0.5894 for x = 0.0, 0.2, 0.4, 0.6, and 0.8, respectively. That $b > 0.5$ for all electrodes indicates both diffusion-controlled and surface-controlled reactions [54]. Moreover, in Figure 5f, the lower value of the scan rate region has a linear dependence relation with the square root of the scan rate; this indicates a quasi-reversible electrochemical reaction [65]. Figure 5f also indicates that, at a higher scan rate > 100 mV/s, the ion diffusion is limited to the surface of the active material of the electrode, i.e., EDLC dominates the pseudocapacitor, and diffusion of OH^- ions can adhere only to the outer layer of the nanostructure, which contributes less to the electrochemical capacitive behavior [66]. On the other hand, the Faradaic redox reaction dominates at scan rates < 100 mV/s due to more effective usage of the working electrode's active material [67]. Moreover, the diffusion of OH^- ions can easily penetrate deep into the nanostructure's interlayer, which leads to adsorption of more ions and hence ends up with higher specific capacitance [68].

The capacitive and diffusion processes are the two mechanisms for current response at a fixed potential [69,70]. The equation below gives their contributions [71].

$$C_{sp} = k_1 + {k_2}^{-1/2} \tag{3}$$

k_1 and k_2 are determined from the C_{sp} vs.$V^{-1/2}$ linear plot, where k_2 is the slope and k_1 is the intercept. k_1 indicates diffusion and k_2 capacitance contribution to the total specific capacitance for a given voltage. For the calculation, the specific capacitance is plotted against the slow scan rate up to a value of 20 mV/s and performed a regression fit using Equation (3). The obtained value for k_1 and k_2 was used to determine the fractional contribution in terms of diffusion and capacitance from total specific capacitance [72], as given in Figure 5g. Figure 5g shows that the contribution to the current response at a fixed potential is more diffusive than capacitive and decreases with the Al content.

To further estimate the potential application of as-prepared electrodes for supercapacitors, the galvanostatic charge-discharge (GCD) measurement was performed. GCD was measured within the voltage window of 0.0 to 0.6 at different current densities between 1 A/g to 30 A/g in 3 M KOH solution are given in Figure 6a–e. These figures indicate that prepared electrodes of $Ni_{1-x}Al_xCo_2O_4$ can charge and discharge rapidly with good electrochemical reversibility at different constant current densities. As in CV curves, the non-linear relationship between the potential and time in both the charge-discharge cycle indicates the capacitance of studied nanomaterials is not constant in between the potential range and reflects typical PCs behavior [73]. The non-linearity of the GCD curve is a consequence of the Co^{3+}/Co^{4+}, and Ni^{2+}/Ni^{3+} ions redox reactions with OH^-. The discharge process occurs in three distinct steps. First, there is a rapid potential drop that occurs owing to the internal resistance. The second is a slow potential decay at an intermediate time, which is due to the Faradaic redox reaction. The third is a fast potential decay which is created by electric double layer capacitance [74]. The specific capacitance values for electrodes of $Ni_{1-x}Al_xCo_2O_4$ were calculated by using Equation (4) [75].

$$C_{sp} = \frac{I * t}{m * \Delta V} \tag{4}$$

where C_{sp} is the specific capacitance (F/g), I (A) is the charge-discharge current, ΔV (V) is the potential range, m (g) is the mass of the electroactive materials and t (s) is the discharging time.

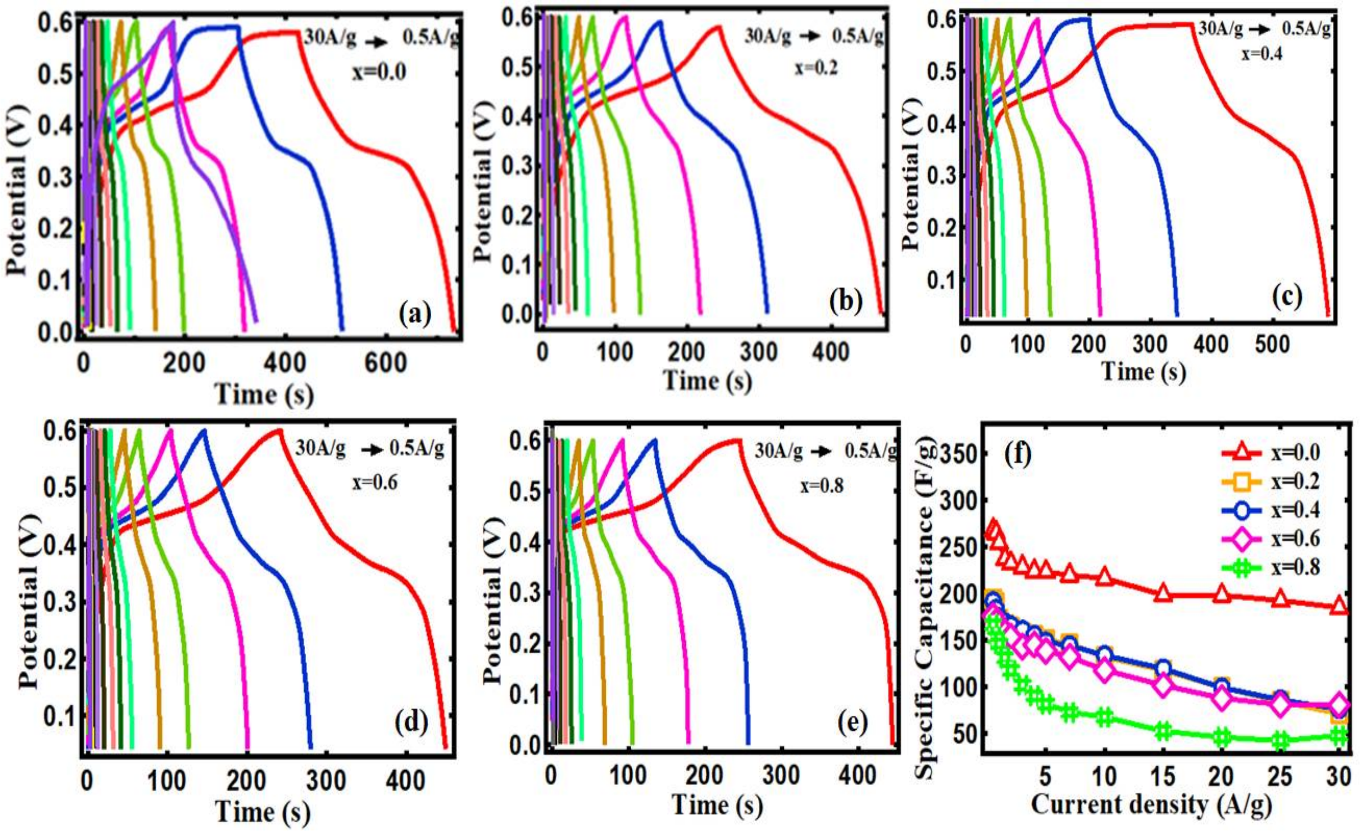

Figure 6. (**a**–**e**) Charge-discharge curves of $Ni_{1-x}Al_xCo_2O_4$, electrode measured in the current density window of 0.75 to 30 A/g under 3 M KOH electrolytes. Figure (**f**) Comparison of specific capacitance as a function of current density.

The pseudocapacitance behavior of electrodes with respect to their discharging time is confirmed by the presence of voltage plateau on GCD curves [76]. The specific capacitance values of $Ni_{1-x}Al_xCo_2O_4$ were calculated using Equation (4) at 0.5 A/g are 268, 194, 192, 176, and 167 F/g for x = 0.0, 0.2, 0.4, 0.6, and 0.8, respectively, and are listed in Table 4. Figure 6f shows the dependence of current density with specific capacitance. A decrease in the specific capacitance with the increase of the discharge current is caused by the insufficient time available for the diffusion of the electrolyte ions into the inner electrode surface and the increase of the potential drop towards higher discharge currents [77].

Table 4. Data of specific capacitance obtained from cyclic voltammetry, specific capacitance obtained from charge-discharge curves, energy density, and power density for $Ni_{1-x}Al_xCo_2O_4$.

x, Content	Specific Capacitance at 2 mv/s (F/g)	Specific Capacitance at 0.5 A/g (F/g)	Energy Density (Wh/Kg)	Power Density (W/Kg)
0.0	512	268	12.4	6316.6
0.2	368	194	8.9	6289.1
0.4	371	192	9.1	5281.2
0.6	380	176	8.7	6670.9
0.8	356	167	8.2	4660.4

The cyclic stability of $Ni_{1-x}Al_xCo_2O_4$, x = 0.0, and x = 0.8, electrodes were evaluated by the repeated charge-discharge measurements up to 5000 cycles at a constant current density of 10 A/g and 5 A/g in the potential range between 0.0 and 0.6 V in 3 M KOH, shown in Figure 7a,b respectively. The percentage retention in specific capacitance was calculated using Equation (5) [78].

$$\% \text{ retention in specific capacitance} = (C_{\#}/C_1) \times 100 \tag{5}$$

where $C_{\#}$ and C_1 are specific capacitance at various cycles and the 1st cycle, respectively. Hence, the % retention in specific capacitance after 5000 cycles for $Ni_{1-x}Al_xCo_2O_4$ x = 0.0 and x = 0.8 is 97% and 108.5% respectively. This shows that even after 5000 cycles, the electrode shows outstanding cyclic stability, and hence there is not much high specific capacitance fade from its initial values in x = 0.0. Similarly, in the case of x = 0.8, the specific capacitance improves to 108.5% of its initial value, and this suggests an improvement in the surface moistened by electrolyte ions, access of electrolyte ions up to the pore of electrode materials, and activation of electrodes by electrolyte ions upon cycle repetition [79]. Furthermore, the Coulombic efficiency for x = 0.0 and x = 0.8 is 100% and 99.2%, as shown in Figure 7a,b, respectively.

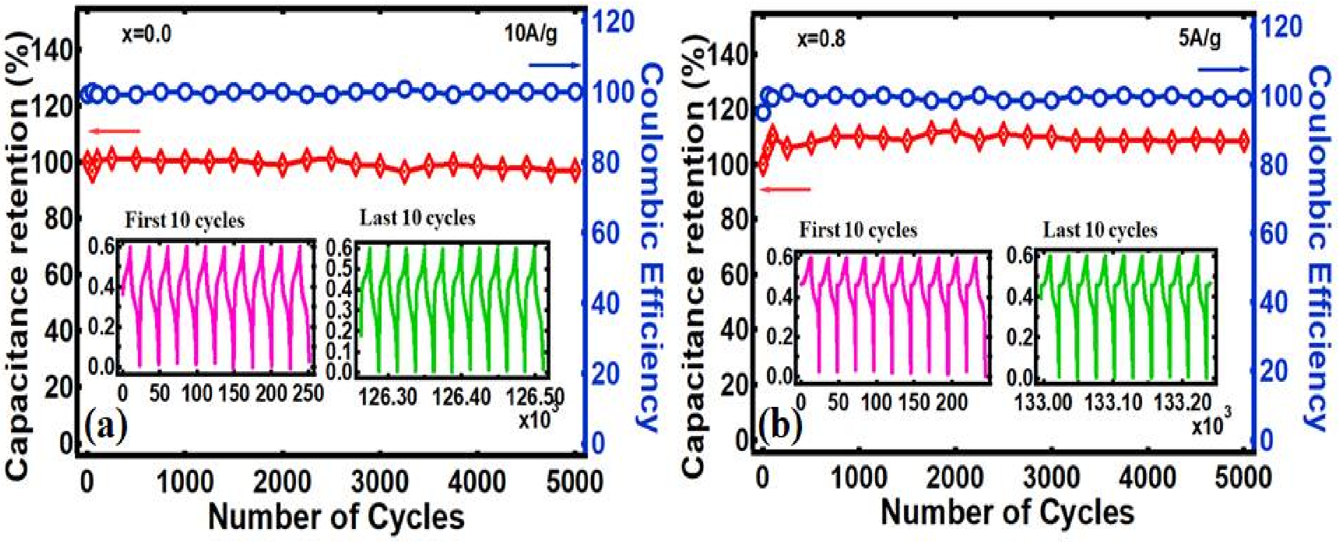

Figure 7. (**a**,**b**) Cyclic stability and Coulombic efficiency tested at 10 A/g and 5 A/g current density up to 5000 cycles in 3 M KOH electrolytes for $Ni_{1-x}Al_xCo_2O_4$, x = 0, and x = 0.8.

Ragone plots of synthesized $Ni_{1-x}Al_xCo_2O_4$ are given in Figure 8a. The energy (E) and power (P) densities are determined using the equations below [32],

$$E = (1/2)CV^2 \tag{6}$$

$$P = E/t \tag{7}$$

where C is the electrodes' specific capacitance, V is the operating voltage, and the letter t denotes the discharge time in seconds. An excellent-performance supercapacitor must exhibit a high value of both energy density and power density together. Figure 8a shows the superior performance of electrodes with an energy density of up to 12.4 Wh/kg for x = 0.0, with up to a peak power density of 6670.9 W/kg for x = 0.6. Furthermore, Table 5 compares the electrodes' specific capacitances derived from the doping of transition elements on $NiCo_2O_4$ using the hydrothermal method.

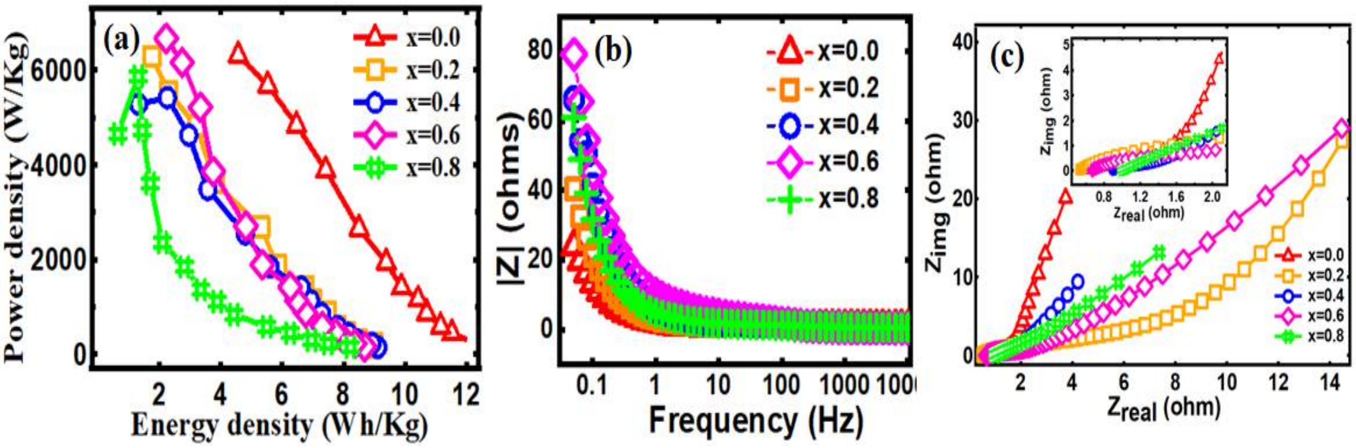

Figure 8. (**a**) Ragone plot of power density vs. energy density, (**b**) frequency-dependent real impedance measured, and (**c**) Nyquist plot for $Ni_{1-x}Al_xCo_2O_4$ at open circuit potential obtained in 3M KOH electrolytes.

Table 5. Comparison of specific capacitance of electrodes derived from doping of transition elements on $NiCo_2O_4$ using the hydrothermal method.

Electrode Material	Scan Rate (mV/s)	Specific Cap. (C_{sp})	Current Density (A/g)	Specific Cap. (C_{sp})	Reference
$Ni_{1-x}Ru_xCo_2O_4$ (x = 0.00, 0.02, 0.05, 0.10, 0.20)	—	—	1	831 F/g, 913 F/g, 1004 F/g, 1527 F/g, 1483 F/g	[27]
$Ni_{1-x}Mn_xCo_2O_4$ (x =1.0, 0.7, 0.5, 0.3, 0.0)	—	—	1	243 F/g (x = 0.3), 366 F/g (x = 0.5, max), 162 F/g (x = 0.7)	[28]
$Ni_{1-x}Zn_xCo_2O_4$ (x = 0.5)	—	—	2	1228 F/g	[30]
$Ni_{1-x}Fe_xCo_2O_4$ (x = 1)	—	—	1	2237 F/g at 1 h,2208 F/g at 3 h, 1976 F/g at 5 h.	[31]
$Ni_{1-x}Ca_xCo_2O_4$ (x = 0.0, 0.2, 0.4, 0.6, 0.8)	2	506 F/g,508 F/g, 355 F/g, 934 F/g, 571 F/g	0.5	284 F/g, 365 F/g, 317 F/g, 558 F/g, 253 F/g	[32]
$Ni_{1-x}Al_xCo_2O_4$ (x = 0.0, 0.2, 0.4, 0.6, 0.8)	2	512 F/g,368 F/g, 371 F/g, 380 F/g, 356 F/g	0.5	268 F/g, 194 F/g, 192 F/g, 176 F/g, 167 F/g	[This study]

The superior electrochemical performance of as-synthesized $Ni_{1-x}Al_xCo_2O_4$ nanostructure electrode materials was further confirmed by the electrochemical impedance spectroscopy (EIS) measurement held at 10 mV AC perturbation in the frequency range from 10 kHz to 0.05 Hz. Figure 8b shows the tendency of the real part of the impedance (Z′) to decrease with increasing frequency for all samples. When x = 0.0, it has the lowest real part of the impedance. The magnitude of the real part of the impedance (Z′) increases as Al^{3+} content increases, which affects the rise of grains, grain boundaries, and electrode interface resistance. Figure 8c shows the Nyquist plots for all of the $Ni_{1-x}Al_xCo_2O_4$ nanostructures. In this plot, the $NiCo_2O_4$ nanostructure electrode exhibits a small semicircle that suggests low internal resistance and charge transfer resistance, and hence this resistance is smaller than Al^{3+} doped $NiCo_2O_4$. Towards higher frequencies, the real part (Z_{real}) of the impedance represents a combined resistance of contact resistance at active material/current collector interface, ionic resistance of the electrolyte, and intrinsic resistance of the nanomaterials used in the electrode [80]. The semicircle at the high-frequency range is due to the Faradaic charge transfer resistance (R_{ct}) of the redox reaction between the electrode and electrolyte. The decrease in the diameter of the semicircle indicates lower charge transfer resistance [81]. These variations of the EIS curve from semicircle towards higher frequencies and linearity towards lower frequencies relate to reversible Faradaic redox reaction and access of OH^- ions into the pore of the electrode material. This behavior of the EIS curve describes the PCs properties of the prepared $Ni_{1-x}Al_xCo_2O_4$ nanostructure electrode [82]. The slope of the 45° portion of the curve is called Warburg resistance (Z_w) and results from the frequency dependence of ion diffusion/transport in the electrolyte to the electrode surface [83,84]. The Nyquist plot is a vertical line for an ideal electrode material, and more is the vertical line represents better electrolyte diffusion and capacitive behavior [85]. Figure 8c shows that R_{ct} is smaller for $NiCo_2O_4$ and has a more vertical line, which offers better rate capability.

First-principles density functional theory (DFT) calculations were performed using VASP^2 [34] (Vienna ab initio simulation package) with the projected augmented wave (PAW) [35] type pseudo-potential and the plane-wave basis set. The exchange and correlation part for the HSE calculations was described by hybrid functional [36] containing a 40% Hartree-Fock exchange. Here, we used a 4 × 4 × 2 k-points mesh centered at the Gamma point with a plane wave cutoff of 400 eV, which is enough for the self-consistent calculation. The global break condition for the electronic and ionic self-consistent (SC) loop was set to be 10^{-4} eV and 10^{-3} eV, respectively. In our calculation, we dealt with a cell containing 28 atoms as a total. The value of gaussian smearing was adjusted to be 0.20. Even though the ratio of x is 20% in the experiment, we chose 25% in the calculations because changing it to 20% would require a much larger supercell, which eventually increases the computing time and memory excessively. Figure 9a shows the side view along the *x*-axis of the crystal structure of $Ni_{1-x}Al_xCo_2O_4$, while Figure 9b shows the band-gap variation from 2.42 eV to 4.82 eV for the different values of x. For the system without Al atom, which is $Ni_1Co_2O_4$, the band gap was found at 2.42 eV, which agrees with the previously reported experimental values of 2.06 eV [86] and 2.64 eV [87]. This value is the minimum among all the cases of adding Al to the system. Adding an Al atom above 0.8, the band-gap reached its maximum value of 4.82 eV for the case where Al completely replaces Ni, as shown in Figure 9a. These results suggest that the energy band-gap of $Ni_{1-x}Al_xCo_2O_4$ remains largely unaltered ($x < 0.8$) with the Al^{3+} substitution, which translates to the fact that the electrical conductivity of $Ni_{1-x}Al_xCo_2O_4$ could remain unaltered with the Al^{3+} substitution below $x = 0.8$. In the absence of the contribution of electrical conductivity to the electrochemical performance of $Ni_{1-x}Al_xCo_2O_4$, at least for $x < 0.8$, it can be concluded that the electrochemical performance of $Ni_{1-x}Al_xCo_2O_4$ could be dictated by other factors, such as morphology, the oxidation potential of participating ions, active metal sites, and the internal resistance of the compound.

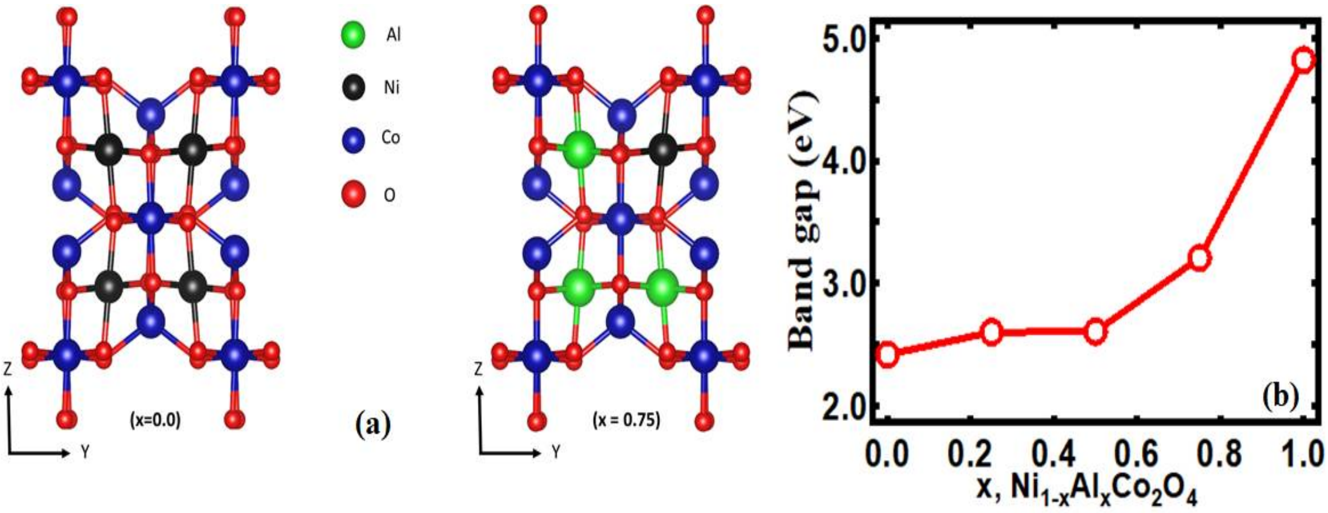

Figure 9. (**a**) Side view, along the x-axis of the crystal structure and (**b**) energy band-gap of $Ni_{1-x}Al_xCo_2O_4$ obtained from DFT calculations as a function of content, x.

4. Conclusions

Finally, a simple and cost-effective technique was developed to report the effect of Al^{3+} doping on the structural and electrochemical performance of the $NiCo_2O_4$ nanostructure. The experimental results revealed the dependence of surface area, specific capacitance, and electrochemical performance of $NiCo_2O_4$ on Al^{3+} content. The doped compound's overall electrochemical performance, viz. energy and power density, was observed to be significantly superior to other doped $NiCo_2O_4$ compounds. The DFT calculation suggests that the energy band-gap of $Ni_{1-x}Al_xCo_2O_4$ (<0.8) remains largely invariant, and hence the electrical conductivity. Thus, the observed reduction in the specific capacitance of doped $Ni_{1-x}Al_xCo_2O_4$ could be attributed to the decrease in active redox sites with Al^{3+} substitution. The study indicates that Al^{3+} can be an excellent cost-effective substitution for expensive cobalt in $NiCo_2O_4$ to provide the desired electrochemical performance. Hence, this work highlights the development of cheaper and more promising electrode doped materials without sacrificing the performance of $NiCo_2O_4$.

Author Contributions: Conceptualization and supervision, S.R.M.; methodology, D.G., data collection and validation. J.C., W.L. and F.A.P.; software, R.B. and X.S.; formal analysis, S.R.M. and R.K.G.; data curation, D.G.; writing—D.G. and X.S.; writing—review and editing, S.R.M. and R.K.G.; supervision, S.R.M.; project administration, S.R.M.; funding acquisition, S.R.M. All authors have read and agreed to the published version of the manuscript.

Funding: Dr. Mishra extends thanks to the FRG grant provided by the University of Memphis, Memphis, TN, USA. Dr. Ram K. Gupta expresses his sincere acknowledgment of the Polymer Chemistry Initiative at Pittsburg State University, Pittsburg, KS, USA, for providing financial and research support for this project.

Institutional Review Board Statement: None.

Informed Consent Statement: Not applicable.

Acknowledgments: Authors acknowledge the Integrated Microscopy Center (IMC) at the University of Memphis for helping with XPS study.

Conflicts of Interest: The authors declare no conflict of interest.

References

1. Zhu, Y.; Pu, X.; Song, W.; Wu, Z.; Zhou, Z.; He, X.; Lu, F.; Jing, M.; Tang, B.; Ji, X. High capacity $NiCo_2O_4$ nanorods as electrode materials for supercapacitor. *J. Alloy. Compd.* **2014**, *617*, 988–993. [CrossRef]
2. Zequine, C.; Ranaweera, C.K.; Wang, Z.; Singh, S.; Tripathi, P.; Srivastava, O.N.; Gupta, B.K.; Ramasamy, K.; Kahol, P.K.; Dvornic, P.R.; et al. High performance and flexible supercapacitors based on carbonized bamboo fibers for wide temperature applications. *Sci. Rep.* **2016**, *6*, 31704. [CrossRef]
3. Yong, S. Fabrication and Characterization of Fabric Supercapacitor. Ph.D. Thesis, University of Southampton, Southampton, UK, 2016.
4. Dubal, D.P.; Gomez-Romero, P.; Sankapal, B.R.; Holze, R. Nickel cobaltite as an emerging material for supercapacitors: An overview. *Nano Energy* **2015**, *11*, 377–399. [CrossRef]
5. Zhi, M.; Xiang, C.; Li, J.; Li, M.; Wu, N. Nanostructured carbon–metal oxide composite electrodes for supercapacitors: A review. *Nanoscale* **2013**, *5*, 72–88. [CrossRef]
6. Han, C.; Xu, X.; Mu, H.; Tian, Q.; Li, Q.; Liu, Y.; Zhang, X.; Zhao, Z.; Su, X. Construction of hierarchical sea urchin-like manganese substituted nickel cobaltite@tricobalt tetraoxide core-shell microspheres on nickel foam as binder-free electrodes for high performance supercapacitors. *J. Colloid Interface Sci.* **2021**, *596*, 89–99. [CrossRef]
7. Zhong, C.; Deng, Y.; Hu, W.; Qiao, J.; Zhang, L.; Zhang, J. A review of electrolyte materials and compositions for electrochemical supercapacitors. *Chem. Soc. Rev.* **2015**, *44*, 7484–7539. [CrossRef]
8. Sarangapani, S.; Tilak, B.V.; Chen, C. Materials for Electrochemical Capacitors: Theoretical and Experimental Constraints. *J. Electrochem. Soc.* **1996**, *143*, 3791. [CrossRef]
9. Huang, L.; Chen, D.; Ding, Y.; Feng, S.; Wang, Z.L.; Liu, M. Nickel–Cobalt Hydroxide Nanosheets Coated on $NiCo_2O_4$ Nanowires Grown on Carbon Fiber Paper for High-Performance Pseudocapacitors. *Nano Lett.* **2013**, *13*, 3135–3139. [CrossRef]
10. Conway, B.E. *Electrochemical Supercapacitors: Scientific Fundamentals and Technological Applications*; Springer Science and Business Media: Berlin/Heidelberg, Germany, 2013.
11. Liu, T.; Pell, W.G.; Conway, B.E. Self-discharge and potential recovery phenomena at thermally and electrochemically prepared RuO_2 supercapacitor electrodes. *Electrochim. Acta* **1997**, *42*, 3541–3552. [CrossRef]

12. Cheng, Q.; Tang, J.; Ma, J.; Zhang, H.; Shinya, N.; Qin, L.-C. Graphene and nanostructured MnO_2 composite electrodes for supercapacitors. *Carbon* **2011**, *49*, 2917–2925. [CrossRef]
13. Yuan, C.; Zhang, X.; Su, L.; Gao, B.; Shen, L. Facile synthesis and self-assembly of hierarchical porous NiO nano/micro spherical superstructures for high performance supercapacitors. *J. Mater. Chem.* **2009**, *19*, 5772–5777. [CrossRef]
14. Ji, J.; Zhang, L.; Ji, H.; Li, Y.; Zhao, X.; Bai, X.; Fan, X.; Zhang, F.; Ruoff, R.S. Nanoporous $Ni(OH)_2$ Thin Film on 3D Ultrathin-Graphite Foam for Asymmetric Supercapacitor. *ACS Nano* **2013**, *7*, 6237–6243. [CrossRef]
15. Moosavifard, S.E.; El-Kady, M.F.; Rahmanifar, M.S.; Kaner, R.B.; Mousavi, M.F. Designing 3D highly ordered nanoporous CuO electrodes for high-performance asymmetric supercapacitors. *ACS Appl. Mater. Interfaces* **2015**, *7*, 4851–4860. [CrossRef]
16. Meher, S.K.; Rao, G.R. Ultralayered Co_3O_4 for High-Performance Supercapacitor Applications. *J. Phys. Chem. C* **2011**, *115*, 15646–15654. [CrossRef]
17. Wang, R.; Yan, X.; Lang, J.; Zheng, Z.; Zhang, P. A hybrid supercapacitor based on flower-like $Co(OH)_2$ and urchin-like VN electrode materials. *J. Mater. Chem. A* **2014**, *2*, 12724–12732. [CrossRef]
18. Dubal, D.P.; Gund, G.; Lokhande, C.D.; Holze, R. Decoration of Spongelike $Ni(OH)_2$ Nanoparticles onto MWCNTs Using an Easily Manipulated Chemical Protocol for Supercapacitors. *ACS Appl. Mater. Interfaces* **2013**, *5*, 2446–2454. [CrossRef]
19. Dubal, D.; Holze, R. A successive ionic layer adsorption and reaction (SILAR) method to induce Mn_3O_4 nanospots on CNTs for supercapacitors. *New J. Chem.* **2013**, *37*, 403–408. [CrossRef]
20. Aricò, A.S.; Bruce, P.; Scrosati, B.; Tarascon, J.-M.; VAN Schalkwijk, W. Nanostructured materials for advanced energy conversion and storage devices. *Mater. Sustain. Energy* **2010**, 148–159. [CrossRef]
21. Bruce, P.G.; Scrosati, B.; Tarascon, J.-M. Nanomaterials for Rechargeable Lithium Batteries. *Angew. Chem. Int. Ed.* **2008**, *47*, 2930–2946. [CrossRef]
22. Wang, G.; Zhang, L.; Zhang, J. A review of electrode materials for electrochemical supercapacitors. *Chem. Soc. Rev.* **2012**, *41*, 797–828. [CrossRef]
23. Zhang, Y.; Li, L.; Su, H.; Huang, W.; Dong, X. Binary metal oxide: Advanced energy storage materials in supercapacitors. *J. Mater. Chem. A* **2015**, *3*, 43–59. [CrossRef]
24. Wang, Q.; Wang, X.; Xu, J.; Ouyang, X.; Hou, X.; Chen, D.; Wang, R.; Shen, G. Flexible coaxial-type fiber supercapacitor based on $NiCo_2O_4$ nanosheets electrodes. *Nano Energy* **2014**, *8*, 44–51. [CrossRef]
25. Shen, L.; Yu, L.; Yu, X.-Y.; Zhang, X.; Lou, X.W. (David) Self-Templated Formation of Uniform $NiCo_2O_4$Hollow Spheres with Complex Interior Structures for Lithium-Ion Batteries and Supercapacitors. *Angew. Chem. Int. Ed.* **2015**, *54*, 1868–1872. [CrossRef]
26. Chakrabarty, S.; Mukherjee, A.; Basu, S. RGO-MoS_2 supported $NiCo_2O_4$ catalyst toward solar water splitting and dye degradation. *ACS Sustain. Chem. Eng.* **2018**, *6*, 5238–5247. [CrossRef]
27. Yang, S.; Yu, J.; Jiang, T.; Zhu, L.; Xu, X. High performance symmetric solid state supercapacitor based on electrode of $RuxNi_{1-x}Co_2O_4$ grown on nickel foam. *J. Alloy. Compd.* **2018**, *764*, 767–775. [CrossRef]
28. Mu, H.; Su, X.; Zhao, Z.; Han, C.; Wang, Z.; Zhao, P. Facile synthesis of $Ni_{0.5}Mn_{0.5}Co_2O_4$ nanoflowers as high-performance electrode material for supercapacitors. *J. Am. Ceram. Soc.* **2019**, *102*, 6893–6903.
29. Uke, S.J.; Akhare, V.P.; Meshram-Mardikar, S.P.; Bodade, A.B.; Chaudhari, G.N. PEG Assisted Hydrothermal Fabrication of Undoped and Cr Doped $NiCo_2O_4$ Nanorods and Their Electrochemical Performance for Supercapacitor Application. *Adv. Sci. Eng. Med.* **2019**, *11*, 357–366. [CrossRef]
30. Gao, K.; Li, S.D. Hollow fibrous $NiCo_2O_4$ electrodes with controllable Zn substitution sites for supercapacitors. *J. Alloy. Compd.* **2020**, *832*, 154927. [CrossRef]
31. Liu, L.; Zhang, H.; Fang, L.; Mu, Y.; Wang, Y. Facile preparation of novel dandelion-like Fe-doped $NiCo_2O_4$ microspheres@nanomeshes for excellent capacitive property in asymmetric supercapacitors. *J. Power Sources* **2016**, *327*, 135–144. [CrossRef]
32. Guragain, D.; Zequine, C.; Bhattarai, R.; Choi, J.; Gupta, R.K.; Shen, X.; Mishra, S.R. Effect of dopant on the morphology and electrochemical performance of $Ni_{1-x}Ca_xCo_2O_4$ ($0 \leq x \leq 0.8$) oxide hierarchical structures. *MRS Adv.* **2020**, *5*, 2487–2494. [CrossRef]
33. Perdew, J.P.; Burke, K.; Ernzerhof, M. Generalized Gradient Approximation Made Simple. *Phys. Rev. Lett.* **1996**, *77*, 3865. [CrossRef]
34. Kresse, G.; Furthmüller, J. Efficient iterative schemes for ab initio total-energy calculations using a plane-wave basis set. *Phys. Rev. B* **1996**, *54*, 11169–11186. [CrossRef] [PubMed]
35. Kresse, G.; Joubert, D. From ultrasoft pseudopotentials to the projector augmented-wave method. *Phys. Rev. B* **1999**, *59*, 1758. [CrossRef]
36. Heyd, J.; Scuseria, G.E.; Ernzerhof, M. Hybrid functionals based on a screened Coulomb potential. *J. Chem. Phys.* **2003**, *118*, 8207–8215. [CrossRef]
37. Chaudhari, S.; Bhattacharjya, D.; Yu, J.-S. Facile Synthesis of Hexagonal $NiCo_2O_4$Nanoplates as High-Performance Anode Material for Li-Ion Batteries. *Bull. Korean Chem. Soc.* **2015**, *36*, 2330–2336. [CrossRef]
38. Sumadiyasa, M.; Manuaba, I. Determining Crystallite Size Using Scherrer Formula, Williamson-Hull Plot, and Particle Size with SEM. *Bul. Fis.* **2018**, *19*, 28–34. [CrossRef]
39. Gonzalo-Juan, I.; Ferrari, B.; Colomer, M. Influence of the urea content on the YSZ hydrothermal synthesis under dilute conditions and its role as dispersant agent in the post-reaction medium. *J. Eur. Ceram. Soc.* **2009**, *29*, 3185–3195. [CrossRef]

40. Hadke, S.; Kalimila, M.T.; Rathkanthiwar, S.; Gour, S.; Sonkusare, R.; Ballal, A. Role of fuel and fuel-to-oxidizer ratio in combustion synthesis of nano-crystalline nickel oxide powders. *Ceram. Int.* **2015**, *41*, 14949–14957. [CrossRef]
41. Adhikari, H.; Ghimire, M.; Ranaweera, C.K.; Bhoyate, S.; Gupta, R.K.; Alam, J.; Mishra, S.R. Synthesis and electrochemical performance of hydrothermally synthesized Co_3O_4 nanostructured particles in presence of urea. *J. Alloy. Compd.* **2017**, *708*, 628–638. [CrossRef]
42. Pan, J.H.; Zhang, X.; Du, A.J.; Bai, H.; Ng, J.; Sun, D. A hierarchically assembled mesoporous ZnO hemisphere array and hollow microspheres for photocatalytic membrane water filtration. *Phys. Chem. Chem. Phys.* **2012**, *14*, 7481–7489. [CrossRef]
43. Zhu, Y.; Ji, X.; Yin, R.; Hu, Z.; Qiu, X.; Wu, Z.; Liu, Y. Nanorod-assembled $NiCo_2O_4$ hollow microspheres assisted by an ionic liquid as advanced electrode materials for supercapacitors. *RSC Adv.* **2017**, *7*, 11123–11128. [CrossRef]
44. Jadhav, A.; Bandal, H.A.; Kim, H. $NiCo_2O_4$ hollow sphere as an efficient catalyst for hydrogen generation by NaBH 4 hydrolysis. *Mater. Lett.* **2017**, *198*, 50–53. [CrossRef]
45. Burt, C.D.; Cabrera, M.L.; Rothrock, M.J.; Kissel, D.E. Urea Hydrolysis and Calcium Carbonate Precipitation in Gypsum-Amended Broiler Litter. *J. Environ. Qual.* **2018**, *47*, 162–169. [CrossRef] [PubMed]
46. Zhi, J.; Wang, Y.; Deng, S.; Hu, A. Study on the relation between pore size and supercapacitance in mesoporous carbon electrodes with silica-supported carbon nanomembranes. *RSC Adv.* **2014**, *4*, 40296–40300. [CrossRef]
47. Kondrat, S.; Perez, C.; Presser, V.; Gogotsi, Y.; Kornyshev, A.A. Effect of pore size and its dispersity on the energy storage in nanoporous supercapacitors. *Energy Environ. Sci.* **2012**, *5*, 6474–6479. [CrossRef]
48. Largeot, C.; Portet, C.; Chmiola, J.; Taberna, P.-L.; Gogotsi, Y.; Simon, P. Relation between the Ion Size and Pore Size for an Electric Double-Layer Capacitor. *J. Am. Chem. Soc.* **2008**, *130*, 2730–2731. [CrossRef]
49. Guragain, D.; Zequine, C.; Poudel, T.; Neupane, D.; Gupta, R.K.; Mishra, S.R. Facile Synthesis of Bio-Templated Tubular Co_3O_4 Microstructure and Its Electrochemical Performance in Aqueous Electrolytes. *J. Nanosci. Nanotechnol.* **2020**, *20*, 3182–3194. [CrossRef]
50. Khairy, M.; Mousa, M. Synthesis of Ternary and Quaternary metal oxides based on Ni, Mn, Cu, and Co for high-performance Supercapacitor. *J. Ovonic Res.* **2019**, *15*, 181–198.
51. Liu, X.; Zhang, Y.; Xia, X.; Shi, S.; Lu, Y.; Wang, X.; Gu, C.; Tu, J. Self-assembled porous $NiCo_2O_4$ hetero-structure array for electrochemical capacitor. *J. Power Sources* **2013**, *239*, 157–163. [CrossRef]
52. Wang, X.; Han, X.; Lim, M.; Singh, N.; Gan, C.L.; Jan, M.; Lee, P.S. Nickel Cobalt Oxide-Single Wall Carbon Nanotube Composite Material for Superior Cycling Stability and High-Performance Supercapacitor Application. *J. Phys. Chem. C* **2012**, *116*, 12448–12454. [CrossRef]
53. Pendashteh, A.; Rahmanifar, M.; Kaner, R.B.; Mousavi, M.F. Facile synthesis of nanostructured $CuCo_2O_4$ as a novel electrode material for high-rate supercapacitors. *Chem. Commun.* **2014**, *50*, 1972–1975. [CrossRef]
54. Kirubasankar, B.; Vijayan, S.; Angaiah, S. Sonochemical synthesis of a 2D–2D $MoSe_2$/graphene nanohybrid electrode material for asymmetric supercapacitors. *Sustain. Energy Fuels* **2019**, *3*, 467–477. [CrossRef]
55. Zou, R.; Xu, K.; Wang, T.; He, G.; Liu, Q.; Liu, X.; Zhang, Z.; Hu, J. Chain-like $NiCo_2O_4$ nanowires with different exposed reactive planes for high-performance supercapacitors. *J. Mater. Chem. A* **2013**, *1*, 8560–8566. [CrossRef]
56. Liu, X.; Long, Q.; Jiang, C.; Zhan, B.; Li, C.; Liu, S.; Zhao, Q.; Huang, W.; Dong, X. Facile and green synthesis of mesoporous Co_3O_4 nanocubes and their applications for supercapacitors. *Nanoscale* **2013**, *5*, 6525–6529. [CrossRef] [PubMed]
57. Ren, J.; Bai, W.; Guan, G.; Zhang, Y.; Peng, H. Flexible and Weaveable Capacitor Wire Based on a Carbon Nanocomposite Fiber. *Adv. Mater.* **2013**, *25*, 5965–5970. [CrossRef]
58. Wei, H.; Zhu, J.; Wu, S.; Wei, S.; Guo, Z. Electrochromic polyaniline/graphite oxide nanocomposites with endured electrochemical energy storage. *Polymer* **2013**, *54*, 1820–1831. [CrossRef]
59. Xu, P.; Gu, T.; Cao, Z.; Wei, B.; Yu, J.; Li, F.; Byun, J.-H.; Lu, W.; Li, Q.; Chou, T.-W. Carbon Nanotube Fiber Based Stretchable Wire-Shaped Supercapacitors. *Adv. Energy Mater.* **2014**, *4*, 1300759. [CrossRef]
60. Ghosh, D.; Giri, S.; Das, C.K. Hydrothermal synthesis of platelet β $Co(OH)_2$ and Co_3O_4: Smart electrode material for energy storage application. *Environ. Prog. Sustain. Energy* **2014**, *33*, 1059–1064. [CrossRef]
61. Guragain, D.; Zequine, C.; Poudel, T.; Neupane, D.; Gupta, R.K.; Mishra, S.R. Influence of Urea on the Synthesis of $NiCo_2O_4$ Nanostructure: Morphological and Electrochemical Studies. *J. Nanosci. Nanotechnol.* **2020**, *20*, 2526–2537. [CrossRef]
62. Augustyn, V.; Come, J.; Lowe, M.A.; Kim, J.W.; Taberna, P.-L.; Tolbert, S.H.; Abruña, H.D.; Simon, P.; Dunn, B. High-rate electrochemical energy storage through Li^+ intercalation pseudocapacitance. *Nat. Mater.* **2013**, *12*, 518–522. [CrossRef]
63. Lindström, H.; Södergren, S.; Solbrand, A.; Rensmo, H.; Hjelm, J.; Hagfeldt, A.; Lindquist, S.-E. Li+Ion Insertion in TiO_2 (Anatase). 1. Chronoamperometry on CVD Films and Nanoporous Films. *J. Phys. Chem. B* **1997**, *101*, 7710–7716. [CrossRef]
64. Zhai, S.; Karahan, H.E.; Wang, C.; Pei, Z.; Wei, L.; Chen, Y. 1D Supercapacitors for Emerging Electronics: Current Status and Future Directions. *Adv. Mater.* **2020**, *32*, e1902387. [CrossRef]
65. Muhammad, H.; Tahiri, I.A.; Muhammad, M.; Masood, Z.; Versiani, M.A.; Khaliq, O.; Latif, M.; Hanif, M. A comprehensive heterogeneous electron transfer rate constant evaluation of dissolved oxygen in DMSO at glassy carbon electrode measured by different electrochemical methods. *J. Electroanal. Chem.* **2016**, *775*, 157–162. [CrossRef]
66. Ali, G.; Fouad, O.A.; Makhlouf, S.; Yusoff, M.; Chong, K.F. Co_3O_4/SiO_2 nanocomposites for supercapacitor application. *J. Solid State Electrochem.* **2014**, *18*, 2505–2512. [CrossRef]

67. Guragain, D.; Zequine, C.; Gupta, R.K.; Mishra, S.R. Facile Synthesis of Bio-Template Tubular MCo_2O_4 (M = Cr, Mn, Ni) Microstructure and Its Electrochemical Performance in Aqueous Electrolyte. *Processes* **2020**, *8*, 343. [CrossRef]
68. Ali, G.A.; Tan, L.L.; Jose, R.; Yusoff, M.M.; Chong, K.F. Electrochemical performance studies of MnO_2 nanoflowers recovered from spent battery. *Mater. Res. Bull.* **2014**, *60*, 5–9. [CrossRef]
69. Liu, T.C.; Pell, W.G.; Conway, B.E.; Roberson, S.L. Behavior of molybdenum nitrides as materials for electrochemical capacitors comparison with ruthenium oxide. *J. Electrochem. Soc.* **1998**, *145*, 1882–1888. [CrossRef]
70. Wang, J.; Polleux, J.; Lim, A.J.; Dunn, B. Pseudocapacitive Contributions to Electrochemical Energy Storage in TiO_2(Anatase) Nanoparticles. *J. Phys. Chem. C* **2007**, *111*, 14925–14931. [CrossRef]
71. Jiao, X.; Hao, Q.; Liu, P.; Xia, X.; Lei, W. Facile synthesis of T-Nb_2O_5 nanosheets/nitrogen and sulfur co-doped graphene for high performance lithium-ion hybrid supercapacitors. *Sci. China Mater.* **2017**, *61*, 273–284. [CrossRef]
72. Wang, H.; Yang, Y.; Li, Q.; Lu, W.; Ning, J.; Zhong, Y.; Zhang, Z.; Hu, Y. Molecule-assisted modulation of the high-valence Co^{3+} in 3D honeycomb-like CoxSy networks for high-performance solid-state asymmetric supercapacitors. *Sci. China Mater.* **2021**, *64*, 840–851. [CrossRef]
73. Fu, H.; Liu, Y.; Chen, L.; Shi, Y.; Kong, W.; Hou, J.; Yu, F.; Wei, T.; Wang, H.; Guo, X. Designed formation of $NiCo_2O_4$ with different morphologies self-assembled from nanoparticles for asymmetric supercapacitors and electrocatalysts for oxygen evolution reaction. *Electrochim. Acta* **2019**, *296*, 719–729. [CrossRef]
74. Hao, C.; Zhou, S.; Wang, J.; Wang, X.; Gao, H.; Ge, C. Preparation of Hierarchical Spinel $NiCo_2O_4$ Nanowires for High-Performance Supercapacitors. *Ind. Eng. Chem. Res.* **2018**, *57*, 2517–2525. [CrossRef]
75. Yu, J.; Fu, N.; Zhao, J.; Liu, R.; Li, F.; Du, Y.; Yang, Z. High Specific Capacitance Electrode Material for Supercapacitors Based on Resin-Derived Nitrogen-Doped Porous Carbons. *ACS Omega* **2019**, *4*, 15904–15911. [CrossRef] [PubMed]
76. Guo, J.; Yin, Z.; Zang, X.; Dai, Z.; Zhang, Y.; Huang, W.; Dong, X. Facile one-pot synthesis of $NiCo_2O_4$ hollow spheres with controllable number of shells for high-performance supercapacitors. *Nano Res.* **2017**, *10*, 405–414. [CrossRef]
77. Qing, X.; Liu, S.; Huang, K.; Lv, K.; Yang, Y.; Lu, Z.-G.; Fang, D.; Liang, X. Facile synthesis of Co_3O_4 nanoflowers grown on Ni foam with superior electrochemical performance. *Electrochim. Acta* **2011**, *56*, 4985–4991. [CrossRef]
78. Mishra, S.; Adhikari, H.; Kunwar, D.; Ranaweera, C.; Sapkota, B.; Ghimire, M.; Gupta, R.; Alam, J. Facile Hydrothermal Synthesis of Hollow Fe_3O_4 Nanospheres: Effect of Hydrolyzing Agents and Electrolytes on Electrocapacitive Performance of Advanced Electrodes. *Int. J. Met. Met. Phys.* **2017**, *2*, 1–15. [CrossRef]
79. Sennu, P.; Aravindan, V.; Lee, Y.-S. High energy asymmetric supercapacitor with 1D@2D structured $NiCo_2O_4$@Co_3O_4 and jackfruit derived high surface area porous carbon. *J. Power Sources* **2016**, *306*, 248–257. [CrossRef]
80. Gamby, J.; Taberna, P.; Simon, P.; Fauvarque, J.; Chesneau, M. Studies and characterisations of various activated carbons used for carbon/carbon supercapacitors. *J. Power Sources* **2001**, *101*, 109–116. [CrossRef]
81. Zequine, C.; Wang, F.; Li, X.; Guragain, D.; Mishra, S.; Siam, K.; Kahol, P.K.; Gupta, R.K. Nanosheets of $CuCo_2O_4$ as a High-Performance Electrocatalyst in Urea Oxidation. *Appl. Sci.* **2019**, *9*, 793. [CrossRef]
82. Jokar, E.; Zad, A.I.; Shahrokhian, S. Synthesis and characterization of $NiCo_2O_4$ nanorods for preparation of supercapacitor electrodes. *J. Solid State Electrochem.* **2014**, *19*, 269–274. [CrossRef]
83. Di Fabio, A.; Giorgi, A.; Mastragostino, M.; Soavi, F. Carbon-poly (3-methylthiophene) hybrid supercapacitors. *J. Electrochem. Soc.* **2001**, *148*, a845–a850. [CrossRef]
84. Wu, M.-S.; Huang, C.-Y.; Lin, K.-H. Electrophoretic deposition of nickel oxide electrode for high-rate electrochemical capacitors. *J. Power Sources* **2009**, *186*, 557–564. [CrossRef]
85. Stoller, M.D.; Park, S.; Zhu, Y.; An, J.; Ruoff, R.S. Graphene-Based Ultracapacitors. *Nano Lett.* **2008**, *8*, 3498–3502. [CrossRef] [PubMed]
86. Bitla, Y.; Chin, Y.-Y.; Lin, J.-C.; Van, C.N.; Liu, R.; Zhu, Y.; Liu, H.-J.; Zhan, Q.; Lin, H.-J.; Chen, C.-T.; et al. Origin of metallic behavior in $NiCo_2O_4$ ferrimagnet. *Sci. Rep.* **2015**, *5*, 15201. [CrossRef] [PubMed]
87. Shi, X.; Bernasek, S.L.; Selloni, A. Formation, Electronic Structure, and Defects of Ni Substituted Spinel Cobalt Oxide: A DFT+U Study. *J. Phys. Chem. C* **2016**, *120*, 14892–14898. [CrossRef]